Tensor Network Path Integral Study of Dynamics in B850 LH2 Ring with Atomistically Derived Vibrations

Amartya Bose*

Department of Chemistry, Princeton University, Princeton, New Jersey 08544

Peter L. Walters†

Department of Chemistry, University of California, Berkeley, California 94720 and
Miller Institute for Basic Research in Science, University of California Berkeley, Berkeley, California 94720‡

The recently introduced multisite tensor network path integral (MS-TNPI) allows simulation of extended quantum systems coupled to dissipative media. We use MS-TNPI to simulate the exciton transport and the absorption spectrum of a B850 bacteriochlorophyll (BChl) ring. The MS-TNPI network is extended to account for the ring topology of the B850 system. Accurate molecular dynamics-based description of the molecular vibrations and the protein scaffold is incorporated through the framework of Feynman-Vernon influence functional. To relate the present work with the excitonic picture, an exploration of the absorption spectrum is done by simulating it using approximate and topologically consistent transition dipole moment vectors. Comparison of these numerically exact MS-TNPI absorption spectra are shown with second-order cumulant approximations. The effect of temperature on both the exact and the approximate spectra is also explored.

I. INTRODUCTION

Photosynthesis in plants, bacteria and algae involves light harvesting complexes. Solar energy creates excitons in these so-called "antenna complexes," which are subsequently transported to the reaction center. Understanding this transport process involves the study of the couplings of the molecular vibrations and the protein scaffold that holds the complex together and their impact on the dynamics. Approximate simulations of these excitation energy transfer (EET) processes are often performed using the Redfield [1] and Förster resonance energy transfer (FRET) [2]. While decent in certain parameter regimes, their accuracy cannot be implicitly assumed. The complexity of simulating quantum dynamics accurately grows exponentially with the number of dimensions. For EET systems, the Hilbert space has a large dimensionality, which consequently makes simulating these systems computationally challenging.

Typically, rigorous wave function-based methods like the density matrix renormalization group (DMRG) [3–7], the multiconfiguration time-dependent Hartree (MCTDH) [8] and its multi-layer extension (ML-MCTDH) [9] have often been used to simulate the dynamics of extended systems. These methods decompose the system using various tensor networks to provide a compressed representation. Though they have been used to study the systems in presence of vibrational manifolds [10], the cost increases with the number of such vibrational modes and the temperature of the simulation. This is because the wave function-based approaches proceed by truncating the basis set corresponding to the bath. In such a framework, incorporating a continuum of such states at a finite temperature becomes computationally very challenging [11].

Quantum systems coupled to vibrational dissipative manifolds are most often simulated using reduced density matrix methods. Foremost among these are the hierarchical equations of motion (HEOM) [11–13] and quasi-adiabatic propagator path integral (QuAPI) [14, 15]. Though historically, HEOM has been exceptionally popular for simulating large quantum systems [16–18], recent work on path integrals [19–22] has made it possible to study these systems as well. Notably, the modular path integral (MPI) [19] has been used to study the exciton transfer in bacteriochlorophyll aggregates [20]. The semi-classical partially linearized density matrix path integral approach along with accurate spectral density have also been used by Lee *et al.* [23] to study the Fenna-Matthew-Olson complex.

We have recently developed a multisite tensor network path integral method (MS-TNPI) [22] using the framework of tensor network path integral [24–27]. MS-TNPI starts with a tensor network decomposition of the system, similar to what is commonly used in DMRG [5, 6, 28, 29] and extends it to incorporate the Feynman-Vernon influence functional [30]. In order to achieve this, the decomposition along the system spatial dimension is extended to the temporal dimension creating a 2D tensor network. It is along this temporal dimension that the influence functional is applied in the form of a matrix product operator (MPO). MS-TNPI, being based on the Feynman-Vernon influence functional, can handle arbitrary spectral densities describing the dissipative environment. The resultant 2D MS-TNPI network can be efficiently contracted to yield the time-dependent reduced density matrix corresponding to the extended quantum system represented in the form of a matrix product state (MPS). This representation contains the full Hilbert space of the

system. Thus, the method is not limited to problems that can only be formulated in the first excitation Frenkel subspace. It allows for simulations of higher order spectra and many-body observables while ensuring that the dissipative medium is still treated in a numerically exact manner.

To accurately simulate the excitonic dynamics in B850, high quality parameterizations of the environment are essential. Much effort has gone into such studies. Starting from simulations of photosynthetic complexes using model spectral densities [1, 31], studies have incorporated descriptions using experiments like fluorescence line narrowing spectra [32, 33] and fully theoretically simulated spectral densities [34–36]. The benefit of using a theoretically simulated spectral density is the internally consistent of treatment the high frequency "quantum" region comprising of rigid vibrations and low frequency "classical" region primarily made of ro-translational modes. Both regions need to be accounted for to obtain accurate dynamics. In this paper, we study the dynamics and absorption spectrum of the exciton transport in the B850 ring of LH2. Molecular dynamics-based descriptions of the dissipative medium coupled to the chlorophyll ring are available in the form of spectral densities [34]. This spectral density captures the effect of the high frequency rigid molecular vibrations as well as the ro-translational modes primarily coming from the protein scaffold using molecular dynamics.

This paper is organized as follows. Section II summarizes the MS-TNPI method and network that is used for the simulations. We describe how the ring conformations can be included after making minor modifications to the propagator. We also show how the absorption spectrum can be calculated using MS-TNPI. This tensor network formulation, utilizing the many-body reduced density matrix corresponding to the extended system, allows a single simulation to give the entire spectrum. Then we discuss the B850 system under study and the simulation results in Sec. III. We analyse the symmetries present in the dynamics and demonstrate the spectra corresponding to different approximations. We also explore the temperature effects on the absorption spectrum under the assumption that the solvent spectral density invariant over the temperature range and show how the behavior of the approximate spectra is qualitatively different. The simulations are computationally quite cheap, probably owing to the structure of the Frenkel model. We also discuss the differences between this model and the well-known Ising model in presence of a dissipative medium. Finally, we end the paper with some concluding remarks in Sec. IV.

II. METHOD

A. Multisite Tensor Network Path Integral

Consider an extended quantum system consisting of P sites coupled with vibrational modes described by the following Hamiltonian:

$$\hat{H} = \hat{H}_0 + \sum_{i=1}^{P} \hat{V}_i \qquad (1)$$

where $\hat{H}_0$ is the Hamiltonian describing the quantum system and $\hat{V}_i$ captures the interaction of the ith site with its local vibrational modes.

For an EET process, the individual system sites are chromophores. The ith site can be represented by the two states, a ground state, $|\phi_i^g\rangle$, and an excited state, $|\phi_i^e\rangle$. The Hamiltonian corresponding to the quantum system consequently can be expressed as a Frenkel model:

$$\hat{H}_0 = \sum_{i=1}^{P} E_i |e_i\rangle\langle e_i| + \sum_{i=1}^{P-1} J_i \left(|e_{i+1}\rangle\langle e_i| + |e_i\rangle\langle e_{i+1}|\right) \quad (2)$$

where

$$|e_i\rangle = |\phi_i^e\rangle \otimes \prod_{j\neq i}^{\otimes} |\phi_j^g\rangle. \qquad (3)$$

Here, $|e_i\rangle$, as expressed by the direct product of the site-local basis in Eq. (3), is the single-exciton state with the excitation localized on the ith site. The electronic excitation energy of the ith system is E_i. Here we have assumed that only the nearest neighbor units are coupled through the coupling J_i. This typically represents a chain. However, B850 is a ring, so there is an extra interaction term between the $i = 1$ and $i = P$ sites, $H_{1,P} = J_P \left(|e_P\rangle\langle e_1| + |e_1\rangle\langle e_P|\right)$.

Under Gaussian response theory, the effect of the dissipative medium can be mapped onto a bath of harmonic oscillators:

$$\hat{V}_i = \sum_l \frac{p_{i,l}^2}{2m_{i,l}} + \frac{1}{2}m_{i,l}\omega_{i,l}^2 \left(x_{i,l} - \frac{c_{i,l}\hat{s}_i}{m_{i,l}\omega_{i,l}^2}\right)^2, \quad (4)$$

where $\omega_{i,l}$ and $c_{i,l}$ are the frequency and coupling of the lth mode of the ith site, respectively. The system operator, $\hat{s}_i$ associated with the ith site, couples the site with its local vibrations. For EETs, the $\hat{s}_i$ operators are typically characterized by $\hat{s}_i |\phi_i^g\rangle = 0$ and $\hat{s}_i |\phi_i^e\rangle = 1$. The site-vibration interaction is described by a spectral density [37, 38]

$$J_i(\omega) = \frac{\pi}{2} \sum_l \frac{c_{i,l}^2}{m_{i,l}\omega_{i,l}} \delta(\omega - \omega_{i,l}), \qquad (5)$$

which is related to the energy-gap autocorrelation function obtained using classical trajectory-based methods.

For the case of the B850 ring, Olbrich and Kleinekathöfer [34] have simulated the correlation function using classical molecular dynamics for the trajectories and ZINDO/S-CIS for the excitation energy. This correlation function on the ith site was subsequently fit

as a sum of exponentials and damped oscillations:

$$C_i(t) = \sum_{j=1}^{N_{\text{exp}}} \eta_j e^{-\gamma_j t} + \sum_{j=1}^{N_{\text{osc}}} \tilde{\eta}_j \cos(\omega_j t) e^{-\tilde{\gamma}_j t} \qquad (6)$$

where N_{exp} is the number of exponentials and N_{osc} is the number of damped oscillations needed to fit the correlation function. Here, η_j is the strength of the jth exponential with a decay rate γ_j. The tildes correspond to the damped oscillations. The spectral density is given as a cosine transform of this correlation function and has the following form [34, 35]:

$$J_i(\omega) = \frac{2}{\hbar} \tanh\left(\frac{\hbar\omega\beta}{2}\right) \int_0^\infty C_i(t) \cos(\omega t)\, \mathrm{d}t \qquad (7)$$

$$= \frac{2}{\hbar} \tanh\left(\frac{\hbar\omega\beta}{2}\right) \left[\sum_{j=1}^{N_{\text{exp}}} \frac{\eta_j \gamma_j}{\gamma_j^2 + \omega^2} \right.$$

$$\left. + \sum_{j=1}^{N_{\text{osc}}} \frac{\tilde{\eta}_j \tilde{\gamma}_j}{2\left(\tilde{\gamma}_j^2 + (\omega - \omega_j)^2\right)} \right] \qquad (8)$$

The correlation functions and thus the spectral densities can, in general, be different for the various sites. However, for B850, due to cylindrical symmetry of the complex, all the spectral densities (and correlation functions) are identical according to Olbrich and Kleinekathöfer [34]. Experimentally, these baths are often reported by their Huang-Rhys factors. Many simulations have been previously done with HEOM using a Drude-Lorentz spectral density [16, 17], which is a specialization of the above form with $N_{\text{exp}} = 1$ and $N_{\text{osc}} = 0$. Of course, such a form is far less flexible in accounting for the full physics of the problem. In particular, it misses out on the contributions from the rigid molecular vibrations.

It should be noted that there are a variety of ways of evaluating quantum correlation functions from purely classical data as summarized in Refs. [39, 40]. It has been recently shown that the so-called harmonic approximation, where the hyperbolic tangent is replace by its high temperature limit, yields better agreement with the quantum correlation function. It has also been shown to better maintain the temperature independence of the spectral density [41]. Additionally, the approach employed by Olbrich and Kleinekathöfer [34] suffers from the "geometry mismatch" problem, i.e., the potential surface used for the classical molecular mechanics (MM) part of the simulation does no have the same normal modes and frequencies as the corresponding quantum potential. In particular, it has been shown that for a gas phase BChl molecule the frequencies predicted by the MM surface are at substantially higher then those corresponding to the quantum surface [42]. Newer methods of calculating spectral densities designed to remedy these issues are available [36, 42]. It is not entirely clear to what extent these deficiencies in the spectral density effect observables like the population dynamics and spectra. As

MS-TNPI is derived completely independently from the spectral density used, it offers an excellent means to investigate the effects of these improved spectral densities on observables of interest. While not done here, this will be the topic of future research.

The reduced density matrix of the extended quantum system can be represented as a path integral expression:

$$\tilde{\rho}(S_N^\pm, N\Delta t) = \text{Tr}_{\text{bath}} \left\langle S_N^+ \middle| \rho(N\Delta t) \middle| S_N^- \right\rangle \qquad (9)$$

$$= \sum_{S_0^\pm} \sum_{S_1^\pm} \cdots \sum_{S_{N-1}^\pm} \tilde{\rho}(S_0^\pm, 0) P_{S_0^\pm \cdots S_N^\pm} \qquad (10)$$

$$= \sum_{S_0^\pm} \sum_{S_1^\pm} \cdots \sum_{S_{N-1}^\pm} \tilde{\rho}(S_0^\pm, 0) P^{(0)}_{S_0^\pm \cdots S_N^\pm} F\left[\left\{S_n^\pm\right\}\right] \qquad (11)$$

where $\tilde{\rho}$ is the reduced density matrix at an arbitrary time, $P_{S_0^\pm \cdots S_N^\pm}$ is the path amplitude tensor, $P^{(0)}_{S_0^\pm \cdots S_N^\pm}$ is the bare path amplitude tensor and F is the Feynman-Vernon influence functional [30]. The system states at the nth time point are collectively denoted by $S_n^\pm$. (The superscript of "$\pm$" denotes the combined forward-backward state, with the "$+$" and "$-$" coordinates defining the bra and ket sides of the reduced density matrix respectively. The state of the ith site at the nth time point will be denoted by $s_{i,n}^\pm$. In these notations, the first index will be the spatial index and the second index will be the temporal one. The forward-backward state of the ith site, $s_{i,n}^\pm$, can take values corresponding to $|\phi_i^g\rangle\langle\phi_i^g|$, $|\phi_i^g\rangle\langle\phi_i^e|$, $|\phi_i^e\rangle\langle\phi_i^g|$, or $|\phi_i^e\rangle\langle\phi_i^e|$.) The key terms appearing here are the bare path amplitude tensor, the influence functional and the path amplitude tensor. The bare path amplitude tensor, $P^{(0)}_{S_0^\pm \cdots S_N^\pm}$, contains the full information of the system independent of the solvent. It is given by:

$$P^{(0)}_{S_0^\pm \cdots S_N^\pm} = K(S_0^\pm, S_1^\pm, \Delta t) K(S_1^\pm, S_2^\pm, \Delta t)$$

$$\times \cdots K(S_{N-1}^\pm, S_N^\pm, \Delta t), \qquad (12)$$

where K is the so-called "forward-backward propagator" obtained from a direct product of the forward, U, and backward, $U^\dagger$, system propagators,

$$K(S_n^\pm, S_{n+1}^\pm, \Delta t) = U(S_n^+, S_{n+1}^+, \Delta t)\, U^\dagger(S_n^-, S_{n+1}^-, \Delta t). \qquad (13)$$

The influence functional, F, encodes the interaction of the system with the solvent. Since the vibrational modes are site local, it can be expressed as a product of site-specific influence functionals:

$$F\left[\left\{S_n^\pm\right\}\right] = \prod_{i=1}^P F_i\left[\left\{s_{i,n}^\pm\right\}\right], \qquad (14)$$

where

$$F_i\left[\left\{s_{i,n}^\pm\right\}\right] = \exp\left(-\frac{1}{\hbar} \sum_k \Delta s_{i,k} \sum_{k' \le k} \left(\text{Re}\left(\eta_{k,k'}^i\right) \Delta s_{i,k'}\right.\right.$$

$$+2i \, \mathrm{Im} \left(\eta^i_{k,k'} \right) \bar{s}_{i,k'} \bigg) . \tag{15}$$

The bath response function, $C_i(t)$ in Eq. (6), discretized along the QuAPI system path [14, 15] for the ith site is given by $\eta^i_{kk'}$. Additionally, $\Delta s_{i,k} = s^+_{i,k} - s^-_{i,k}$ and $\bar{s}_{i,k} = \frac{1}{2} \left(s^+_{i,k} + s^-_{i,k} \right)$. (The method is, of course, not tied down to any specific form of the spectral density like the Drude or the Ohmic forms. The η-coefficients can be expressed in terms of integrals over the spectral density.) Because the B850 ring necessitates identical spectral densities, the η-coefficients are the same for every site. The path amplitude tensor, $P_{S^\pm_0 \cdots S^\pm_N}$ is effectively the product of the bare path amplitude tensor and the influence functional. It contains the full information of the system embedded in the solvent.

To simplify the discussion, let us briefly neglect the effects of the solvent. Under this condition, the summations in Eq. (11) can be performed independently, since the influence functional, which couples the system at different time points, is omitted when there is no system-solvent interactions. In this case, the density matrix can be evaluated iteratively,

$$\tilde{\rho}(S^\pm_n, n\Delta t) = \sum_{S^\pm_{n-1}} \tilde{\rho}(S^\pm_{n-1}, (n-1)\Delta t) K(S^\pm_{n-1}, S^\pm_n, \Delta t). \tag{16}$$

This has the same form as matrix-vector multiplications. The storage and computational complexity of these expressions grow exponentially with the number of system sites making direct simulations of extended systems practically impossible. However, for many extended systems, the correlations between system sites decrease rapidly with the distance between them. Thus, the large tensors (e.g., $\tilde{\rho}$ and K) representing every particle in the system can be efficiently factored into a network of smaller tensors corresponding to a single particle each. This fact is widely utilized by methods like time-dependent DMRG [43] and time-dependent variational principal (TDVP) [44, 45]. In this representation, the reduced density matrix becomes an MPS,

$$\tilde{\rho} \left(S^\pm_n, n\Delta t \right) = \sum_{\{\alpha_{(i,n)}\}} A^{s^\pm_{1,n}}_{\alpha_{(1,n)}} A^{s^\pm_{2,n}}_{\alpha_{(1,n)},\alpha_{(2,n)}} \cdots A^{s^\pm_{P,n}}_{\alpha_{(P-1,n)}}, \tag{17}$$

the forward-backward propagator an MPO,

$$K \left(S^\pm_n, S^\pm_{n+1}, \Delta t \right) = \sum_{\{\alpha_{(i,n)}\}} W^{s^\pm_{1,n}, s^\pm_{1,n+1}}_{\alpha_{(1,n)}} W^{s^\pm_{2,n}, s^\pm_{2,n+1}}_{\alpha_{(1,n)},\alpha_{(2,n)}} \cdots W^{s^\pm_{P-1,n}, s^\pm_{P-1,n+1}}_{\alpha_{(P-2,n)},\alpha_{(P-1,n)}} W^{s^\pm_{P,n}, s^\pm_{P,n+1}}_{\alpha_{(P-1,n)}}, \tag{18}$$

(a) MPS representation of the density matrix
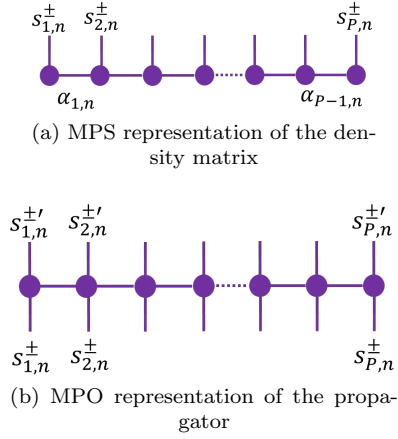

(b) MPO representation of the propagator

FIG. 1. Matrix product representations of the density matrix and the propagator.

and the matrix-vector multiplication becomes an MPO-MPS application. Here, $\alpha_{i,n}$ is the "bond" index that connects the ith site at time-step n to the $(i+1)^{\mathrm{th}}$ site at the same time step. It is called a "spatial" bond index because it connects points that are spatially separated. The structures of the MPS and MPO are shown in Fig. 1. The maximum and average bond dimension associated with the nth time step is $m(n) = \max_i \left(\dim(\alpha_{(i,n)}) \right)$ and $\bar{m}(n) = \frac{1}{P} \sum_i \dim(\alpha_{(i,n)})$, respectively. The efficiency of these factorizations can often be characterized by the maximum bond dimension. Roughly speaking, the smaller the resulting bond dimension the more efficient the MPO/MPS factorization.

For most problems, there are many ways to construct the propagator MPO that often involve a trade off between the maximum time-step and bond dimension. The development of optimal propagator MPOs has been an object of intense research over the years [29, 44–46]. In this work, we use a modified second-order Suzuki-Trotter split propagator MPO that is commonly used with the (second-order) time-evolved block decimation method (TEBD) [4, 43, 47]. These MPOs are generally used to simulate systems with nearest neighbor couplings. For many photosynthetic systems, the ring topology is biologically relevant. As discussed earlier, the ring Hamiltonian has an extra coupling, H_{1P} between the 1$^{\mathrm{st}}$ and the Pth sites. Now, the propagator element between two points S^+_n and S^+_{n+1} for the ring can be written as

$$U_{\mathrm{ring}}(S^+_n, S^+_{n+1}, \Delta t) \approx$$
$$\left\langle S^+_{n+1} \middle| e^{-iH_{1P}\Delta t/2\hbar} U_{\mathrm{chain}}(\Delta t) e^{-iH_{1P}\Delta t/2\hbar} \middle| S^+_n \right\rangle, \tag{19}$$

where U_{chain} is the standard second-order TEBD propagator for the chain. The resulting propagator MPO for the ring is obtained by multiplying the MPOs corresponding to the "long bond," $e^{-iH_{1P}\Delta t/2\hbar}$, together with that of the chain. It is feasible to construct the propagator in a cylindrical form, reflecting the true ring
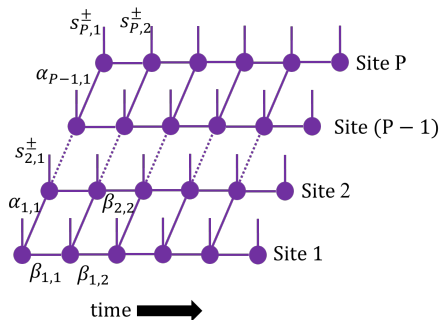
FIG. 2. 2D MS-TNPI tensor network.

FIG. 3. Schematic depiction of the application of the influence functional MPOs to selected sites of the extended system.

symmetry of the system. However, there may be other performance concerns. This would be evaluated in a future work.

The approach discussed till now is a density matrix version of methods like TEBD or time-dependent DMRG. The next step is to incorporate the effects of the solvent by accounting for the time non-locality of the influence functional. Since the different time points can no longer be uncoupled, traditional time step iteration is impossible. In principle, this would cause the computational complexity to increase exponentially with the number of time steps; however, this cost can be avoided by performing an additional DMRG-like tensor decomposition along the time axis [22, 24]. The resulting 2D tensor network, factored in both space and time, forms the foundation of MS-TNPI.

To construct the MS-TNPI network, one starts with the MPO representations of the forward-backward propagator between each of the time-points and uses them to construct a fully factorized tensor network description of the bare path amplitude tensor $P^{(0)}$:

$$P^{(0)}_{S_0^\pm \cdots S_N^\pm} = \sum_{\{\beta_n\}} \mathbb{T}^{S_0^\pm}_{\beta_0} \cdots \mathbb{T}^{S_n^\pm}_{\beta_{n-1}, \beta_n} \cdots \mathbb{T}^{S_N^\pm}_{\beta_{N-1}}. \qquad (20)$$

Here, each $\mathbb{T}$ is in a matrix product representation decomposed along the site axis, and β_n is the bond dimension connecting the tensors at time-point n to the one at $n+1$. These indices are called "temporal" bonds because they connect points on the same site but different times. The 2D structure of the MS-TNPI network is demonstrated in Fig. 18. (For convenience, a more detailed derivation of the tensors that make up $\mathbb{T}$ is provided in Appendix A.) Though Eq. (A8) has been written for the bare path amplitude tensor, the full tensor also would have a practically identical form. The main difference being whether the influence functional has been incorporated.

Since the influence functional has not yet been applied, contracting the 2D MS-TNPI network, as it stands right now, yields the time-evolved density matrix for the isolated extended system expressed in the form of an MPS. Using the tensor network path integral [24], one can define the influence functional MPO for each site or monomer unit and apply it to the corresponding site as illustrated in Fig. 3. The relevant equations for the
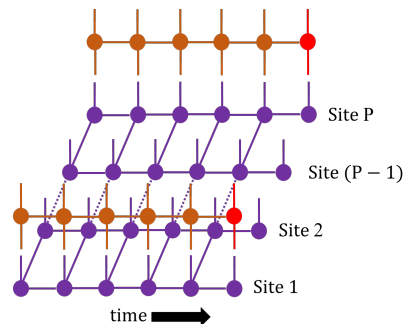
influence functional MPO have been summarized in Appendix B. Now, upon contraction, the network gives the resulting time-evolved reduced density matrix. (Though, we have presumed a lack of correlation between the baths on different sites, it is possible to extend the structure to take correlation effects into account as well by applying operators that connect the "rows" corresponding to the different sites. In absence of those correlation effects, the influence functional MPOs directly affect only the temporal bond dimension and not the spatial bond dimension.)

Let us examine the 2D MS-TNPI network corresponding to the path amplitude tensor in more depth. Along the time axis, it consists of the local path amplitude tensor for each of the sites, effectively generalizing the TNPI structure to multiple sites. On the other hand, along the space axis, each of the "columns" represents the full state of the system at that time point and is effectively a generalization of the reduced density matrix as propagated by time-dependent DMRG methods. The network allows the possibility of many different algorithms for contracting it. While the present work uses a contraction scheme that preserves the columns, and consequently obtains the entire time propagated density matrix as an MPS, future explorations could yield other interesting and performant schemes.

Naïvely speaking, the network should have one column for each time point of propagation. This is due to the non-Markovian memory induced by the bath. This represents the growth of computational cost with the propagation time. Much of this exponential complexity is already controlled through the tensor network decomposition and the accompanying truncated singular value decomposition filtration schemes. However, this is not enough by itself. It is well-known that in condensed phase environments, the memory dies away with the temporal distance between two points. It is, therefore possible to truncate the memory length to say L time-steps and use L as a convergence parameter. This is achieved through a procedure for iterative propagation of the density matrix for the extended system.

When iteration starts, there are L time-steps and, consequently, $L+1$ columns in the MS-TNPI network. These are labeled as C_n for $1 \leq n \leq L+1$. For the initial
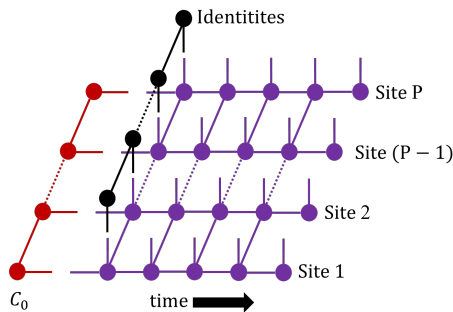
FIG. 4. Schematic illustrating the iteration scheme in the MS-TNPI framework.

step of iteration, let $C_0 = \tilde{\rho}(0)$ written as an MPS. (If, as in Sec. II B, we are simulating a correlation function $C(t) = \text{Tr}\left[U(t)\,\rho(0)\,A\,U^\dagger(t)\,B\right]$, $C_0 = \tilde{\rho}(0)\,A$.) The iteration method can be summarized in the following series of steps. (An MPO-MPS multiplication is written as $\otimes$ in the following steps.)

1. Update C_0 by multiplying it by the MPO C_1. $C_0 \leftarrow C_1 \otimes C_0$. (Note that the first column, C_1, is an MPO and the resulting C_0 an MPS.)

2. Slide all the columns back by one step. $C_j \leftarrow C_{j+1}$ for $j < L$. (Now, the new first column is no longer an MPO and has two temporal bond indices.)

3. Update C_L and insert the C_{L+1} to account for the propagator between the penultimate and the last time steps. (The working equations are in Appendix A.)

4. Apply the influence functional MPO to each row.

5. Trace over the site indices of C_1 to turn it into an MPO again.

Steps (1) – (5) are repeated as many times as required to get the full dynamics. This procedure is schematically represented in Fig. 4.

These calculations involve manipulation of high-dimensioned tensors factorized in different forms. The cost of applying the IF MPO is $\mathcal{O}\left(m_t^3 w_p^2 w_I^2 d^2\right)$, and the cost of the contraction is $\mathcal{O}\left(m^3 w_p^2 m_t\right)$. Here, m_t is the maximum temporal bond dimension, m is the maximum bond dimension of the contracting MPS, w_I is the maximum bond dimension of the IF MPO. The maximum bond dimension of the forward-backward propagator of the bare system is denoted by w_p and $d = 2$ is the dimensionality of a typical system site. The computational cost is linear in the number of sites or system size, which appears as a prefactor in the formal scaling expressions. Though the magnitude of m_t might be dependent on the memory length, L, the exponential growth of complexity within memory is effectively curtailed. The cost propagation beyond the memory span of $\tau = L\Delta t$ is strictly linearly proportional to the number of steps of dynamics beyond the memory length simulated. The dominant

cost is determined by the particular parameters under consideration. For more details about the contractions involved, please consult Ref. [22].

B. Absorption Spectrum

Absorption spectra are calculated as the Fourier transform of dipole-dipole time correlation function,

$$\sigma(\omega) \propto \text{Re} \int_0^t e^{i\omega t} C(t)\, dt \qquad (21)$$

$$C(t) = \text{Tr}\left(\hat{\mu}(t)\hat{\mu}(0)\rho(0)\right). \qquad (22)$$

Here, $\hat{\mu}(t) = \sum_{i=1}^P \hat{U}^\dagger(t)\hat{\mu}\hat{U}(t)$ is the time-evolved total dipole operator, $\hat{\mu} = \sum_{i=1}^P \hat{\mu}_i$. Generally speaking, the local dipole operators do not point in the same direction. Therefore, using the site-local basis, $\hat{\mu}_i = \vec{d}_i(|\phi_i^g\rangle\langle\phi_i^e| + |\phi_i^e\rangle\langle\phi_i^g|)$, where $\vec{d}_i$ is the dipole moment vector corresponding to the ith unit. For calculating the absorption spectrum,

$$\rho(0) = \tilde{\rho}(0) \otimes \prod_i \frac{\exp(-\beta V_i)}{Z_i} \qquad (23)$$

$$\tilde{\rho}(0) = \prod_i^{\otimes} |\phi_i^g\rangle\langle\phi_i^g|, \qquad (24)$$

where the vibrational manifold associated with the ith unit is distributed thermally at an inverse temperature, $\beta = \frac{1}{k_B T}$, on the ground Born-Oppenheimer surface. The partition function for this distribution is given by Z_i.

In the path integral notation of Sec. II A, the correlation function, Eq. (22), can be written as

$$C(N\Delta t) = \sum_{S_0^\pm \ldots S_N^\pm} \sum_{S_0'^\pm} \sum_{S_N'^\pm}$$

$$\delta_{S_N'^+, S_N'^-}\, \tilde{\rho}\left(S_0^\pm, 0\right)\, \hat{\mu}\left(S_0^\pm, S_0'^\pm\right)\, P_{S_0'^\pm \ldots S_N^\pm}\, \hat{\mu}\left(S_N^\pm, S_N'^\pm\right), \qquad (25)$$

where $\hat{\mu}\left(S_n^\pm, S_n'^\pm\right) = \left\langle S_n'^+\left|\hat{\mu}\right|S_n^+\right\rangle \left\langle S_n^-\left|\mathbb{I}_n\right|S_n'^-\right\rangle$ and $\mathbb{I}_n$ represents the identity operator of the full forward-backward space at n^{th} time point. It is worth noting that in this case, the total dipole operator only acts on the forward space; furthermore, it is possible to analytically represent it as an MPO, which is given in Appendix C. Interestingly, in this form, the MPO is extremely compact, having a bond dimension of just two. Since we have an MPO expression for the total dipole operator, the correlation function can be efficiently computed by applying this MPO to the initial density MPS as well as the final time-propagated MPS before taking the trace, as per Eq. (25). By applying the total dipole moment MPO at multiple intermediate points, it should also be possible to calculate higher order response functions at minimal extra computational cost.

From here, we could proceed directly to computing the correlation function. However, the high frequency nature of the electronic absorption necessitates the use of very short time steps, thereby increasing the memory length. Additionally, these correlation functions decay slowly which means the total number of simulation steps would be fairly large. Together, these two factors serve to increase the computational complexity of these simulations. Such a direct approach is, therefore, rather inefficient. Fortunately, though, in this case, it is possible to transform the entire problem into a numerically simpler problem.

This transformation begins by shifting each site by a constant energy term, $\bar{E}$, that has the same order of magnitude as the electronic excitation energy ($\bar{E} \approx 12\,000\,\text{cm}^{-1}$ for B850). The system Hamiltonian, Eq. (2), can then be rewritten as $\hat{H}_0 = \hat{\bar{H}}_0 + \hat{\mathcal{H}}_0$, where

$$\hat{\bar{H}}_0 = \bar{E} \sum_{i=1}^{P} |e_i\rangle\langle e_i| \quad \text{and} \tag{26}$$

$$\hat{\mathcal{H}}_0 = \sum_{i=1}^{P} \epsilon_i |e_i\rangle\langle e_i| + \sum_{i=1}^{P-1} J_i \left(|e_{i+1}\rangle\langle e_i| + |e_i\rangle\langle e_{i+1}|\right), \tag{27}$$

with $\epsilon_i = E_i - \bar{E}$. $\hat{\bar{H}}_0$ commutes with $\hat{\mathcal{H}}_0$, so we can factor $\hat{\bar{U}} = \exp\left(-\frac{i}{\hbar}\hat{\bar{H}}_0 t\right)$ out of the propagator without incurring any Trotter error. Next, we identify the "bra" side of $\hat{\mu}(0)\tilde{\rho}(0)$ (corresponding to the backward path) with the electronic ground state. On the "ket" side, which corresponds to the forward path, it is in a state with a single excitation. Due to the block-diagonal structure of the Frenkel Hamiltonian, the bra of the time-evolving operator remains in the ground state and the ket remains in the manifold of singly excited states. In other words, the backward path remains in the ground state, and forward path only populates the first excited subspace. In this subspace, $\hat{\bar{H}}_0 = \bar{E}$ and $\hat{\bar{U}} = e^{-i\bar{E}t/\hbar}$ Thus, we have:

$$C(t) = e^{-i\bar{E}t/\hbar}\mathcal{C}(t), \tag{28}$$

where $\mathcal{C}(t)$ is the dipole moment autocorrelation function obtained using the propagator $\hat{\mathcal{U}}$ corresponding to $\hat{\mathcal{H}}_0$. Because the extremely high frequency oscillations have been factorized out, the time-steps can now be larger. The multiplication by the fast rotating phase is done as a post-processing step and is equivalent to a shift of the absorption lineshape to account for the redefining of the zero of energy. It is worth noting that since the backward path remains in the ground state, we could have derived a more compressed representation of the influence functional MPO. While this optimization was not needed here, it may be required in the future.

Before concluding this subsection, it is instructive to explore the form of the "initial state". We note that though $\tilde{\rho}(0)$ is a separable state, the initial state, defined as the product with the direct sum of the site local $\hat{\mu}_j$

operators, is surely not separable.

$$\hat{\mu}(0)\tilde{\rho}(0) = \sum_j \hat{\mu}_j \tilde{\rho}(0) \tag{29}$$

$$= \sum_j \vec{d}_j \prod_{k \neq j} I_k \otimes \left(|\phi_j^g\rangle\langle\phi_j^e| + |\phi_j^e\rangle\langle\phi_j^g|\right) \prod_i |\phi_i^g\rangle\langle\phi_i^g| \tag{30}$$

$$= \sum_j \vec{d}_j \prod_{k \neq j} |\phi_k^g\rangle\langle\phi_k^g| \otimes |\phi_j^e\rangle\langle\phi_j^g| \tag{31}$$

where I_k is the identity operator on the kth site. Each of the operators in the summand of Eq. (31) is in a direct product form. This sum over multiple such operators causes the sites to be entangled and the effective initial state to be non-separable. While we have written out the equation explicitly for the absorption spectrum, this issue of non-separability and entanglement of the initial condition is a consequence of the operators involved in the correlation function. This feature is common to most spectra of interest. In fact, for the emission spectrum, the initial condition has even greater entanglement. To our knowledge, MPI is the only other method that is able to use influence functionals for general extended quantum systems; however, since it treats the system sites sequentially, it is not designed to handle non-separable initial states. This means that the simulation would require separate runs, each corresponding to a different term in the sum. The fact that the final result comes from a trace over a non-direct product operator further increases the number of runs that would be be required. Thus, an MPI calculation of the correlation function, given by Eq. (22), is likely many times more costly than a simple calculation of the population dynamics. On the other hand, since MS-TNPI is compatible with the MPS/MPO framework, and the total dipole operator can be expressed as an extremely compact MPO; it can calculate the correlation function at practically the same cost as the population dynamics.

C. A Note About Convergence

As with any numerical approach, the simulations included in this work involve a variety of different convergence parameters. Here, we give a brief description of the key parameters as well as a quick outline of the procedure used. Loosely speaking, these parameters can be grouped into two categories: those arising from the path integral (i.e., time-step and memory length) and those coming from the SVD compression of the network. Under our compression scheme, the singular values, λ_n, are discarded such that

$$\frac{\sum_{n \in \text{discarded}} \lambda_n^2}{\sum_n \lambda_n^2} < \chi. \tag{32}$$

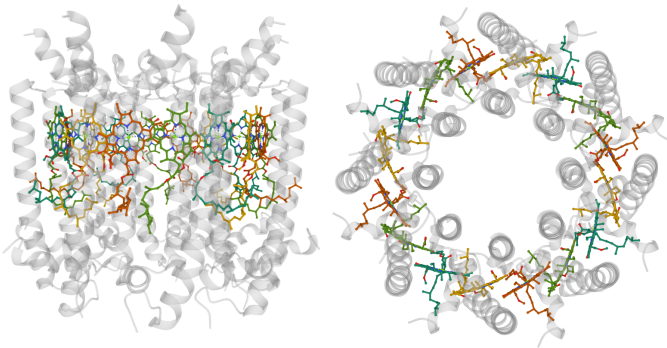The particular value of truncation threshold, χ, used depends on the part of the network being compressed. We

FIG. 5. Side and top views of the B850 ring of LH2. The molecular vibrations and the protein scaffolding affect the dynamics.

FIG. 6. Spectral density corresponding to the B850 ring as calculated in Ref. [34].

used two different truncation thresholds, here, χ_t (used for compressing the bonds along the temporal axis) and χ_s (for the spatial axis). Conceptually, the value of χ_t changes with the memory length, L, while the value of χ_s changes with the number of sites and the strength of the couplings between them. Of course, while doing the calculation, these clean conceptual divisions do not hold and the two dimensions start affecting each other.

Typically, one starts by choosing a particular value of time-step and L, and iterating through different cutoffs to achieve convergence with respect to them. Subsequently, the time-step and L are changed, repeating the process of converging the cutoffs at each step, to find the largest converged time-step and the smallest L. Unlike typical system-solvent decomposed methods, here, the Trotter error caused by the time-step stems from both the system-solvent split as well as the system-system split. The memory length, L, however is only caused by the local baths.

III. RESULTS

The B850 ring of LH2, shown in Fig. 5, is an important component of photosynthetic complexes. It has been previously studied with approximate spectral densities. Here, we use the accurate spectral densities derived by Olbrich and Kleinekathöfer [34] to model the interaction of the system with the rigid molecular vibrations and the impact of the protein scaffolding. The resultant spectral density obtained along MD trajectories with ZINDO/S-CIS calculations for the energy gap is shown in Fig. 6. It is well-known that the B850 ring can be decomposed into constituent dimers with high intra-dimer electronic couplings. The couplings between the different dimers is considerably smaller. The electronic couplings between the nearest neighbors, calculated using the method of transition charges from electrostatic potentials (TrEsp), [48, 49] alternate between $173\,\mathrm{cm^{-1}}$ and $140\,\mathrm{cm^{-1}}$ [34]. Notably, these values are significantly less than ones derived from experiments because they take

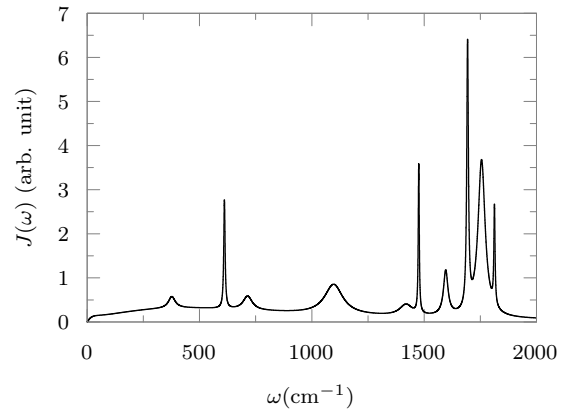environmental screening effects into account. As a point of comparison and to understand the system better, we also consider the experimentally derived electronic couplings of $315\,\mathrm{cm^{-1}}$ and $245\,\mathrm{cm^{-1}}$ as reported by Freiberg *et al.* [50] in their experimentally fit models. These parameters have been used by Strümpfer and Schulten [17] in their study of the dynamics of B850 ring coupled with a Drude-Lorentz spectral density. Other experimentally derived numbers [51] are also of similar magnitude.

The dynamics of exciton transport in the B850 ring corresponding to the initial excitation of the 8$^{\text{th}}$ BChl unit ($\tilde{\rho}(0) = |e_8\rangle\langle e_8|$) with the TrEsp couplings is shown in Fig. 7. For the calculations shown in here, typically $\Delta t = 4.84\,\mathrm{fs}$ yields converged results with a memory span of $L\Delta t = 24.19\,\mathrm{fs}$. The cutoffs for this problem are very different along the temporal and spatial axes. Along the time-axis, χ_t converged around 10^{-10} whereas the spatial cutoff, χ_s was converged around $10^{-5} - 10^{-7}$. A representative converged simulation of the full dynamics takes around 6 hours on an Intel® Xeon® Gold CPU. The runtime is, of course, extremely dependent on the exact parameters of the system under study and the levels of singular value decomposition truncation that is being done. Because of the low couplings, the first peak of the initially excited site happens at $\approx 75\,\mathrm{fs}$, which is significantly later than what is expected from experimentally derived couplings. As a comparison, we demonstrate the corresponding dynamics of B850 ring parameterized by experimentally derived electronic couplings in Fig. 8. Notice that in this case, the prominent hump in the excited state population of the initially excited monomer happens around $37\,\mathrm{fs}$.

The dynamics of the dimerized ring of identical chlorophyll molecules displays an interesting symmetry. Consider all pairs of BChl units equidistant from the initially excited one, which in this case is the 8$^{\text{th}}$ unit. If the electronic couplings between all nearest neighbor pairs were equal, the dynamics of the monomers of any pair would have been identical. However, because of the alternat-
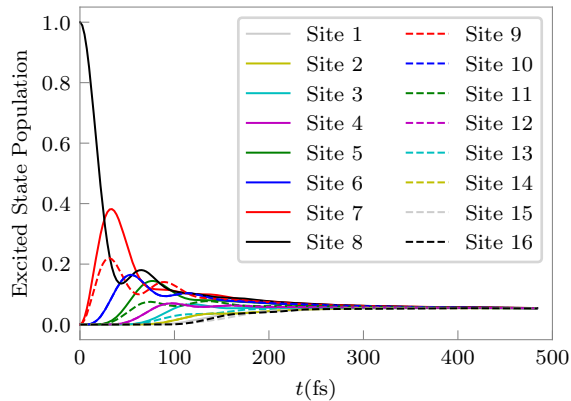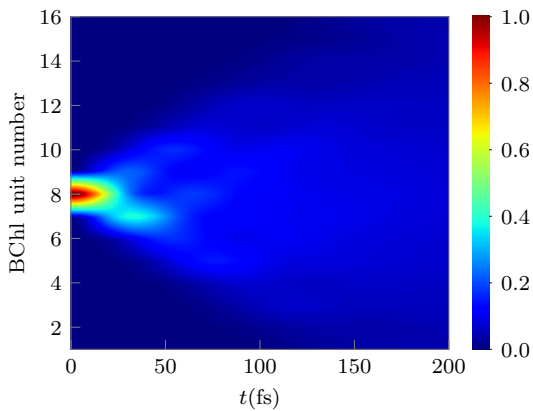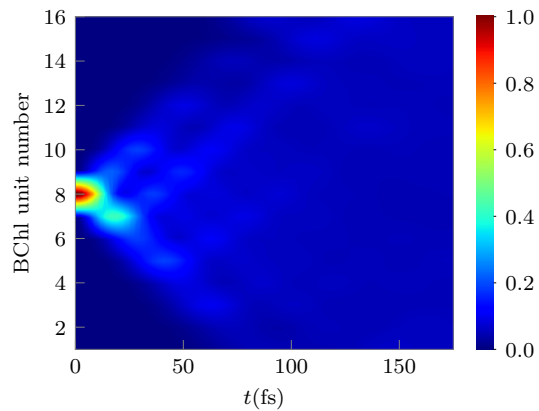
(a) Excited state populations of each of the BChl sites.
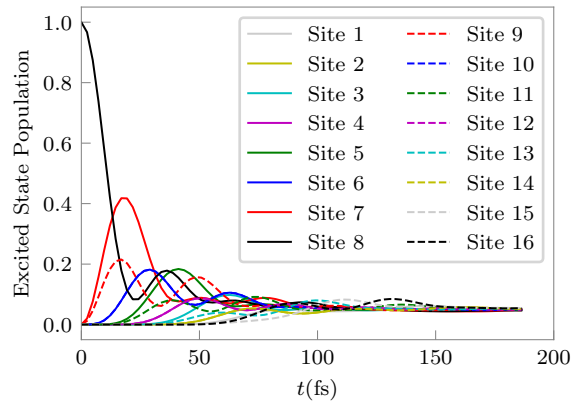
(b) 2D plot of the transfer of excitations from one BChl site to another.

FIG. 7. Excited states of the bacteriochlorophyll corresponding to the B850 ring with the TrEsp couplings.

(a) Excited state populations of each of the BChl sites.

(b) 2D plot of the transfer of excitations from one site to another.

FIG. 8. Excited states of the bacteriochlorophyll corresponding to the B850 ring with the experimentally derived couplings.

ing nature of these couplings, such a symmetry would be absent. Interestingly, this situation leads to a different symmetry. Now it is every alternate pair that has identical dynamics and the other pairs have different dynamics. Of course, because the number of units in this case is even, the unit diametrically opposite to the initially excited unit, the 8th BChl unit in this case, is unique.

Now, let us compare the dynamics of the dimerized BChl ring with the TrEsp couplings with a BChl ring with all the couplings set at the average value of the TrEsp couplings. Figure 9 shows the dynamics corresponding to the non-dimerized (with average couplings, Fig. 9 (a)) and dimerized (alternating couplings, Fig. 9 (b)) ring. Note that in Fig. 9 (a), all the lines but the ones corresponding to 8 and 16 are paired. For example, the dynamics corresponding to the 7th and the 9th sites are identical (they have the same colors in the figure, but different line styles, so it seems like there is only one single line). The same applies to the dynamics of the 6th and the 10th sites. However, as discussed, this is not the case in Fig. 9 (b). For this case, the dynamics

of site 7 and site 9 are different, as is the dynamics of site 5 and 11. However the dynamics of site 6 is same as that of site 10, as is the dynamics of sites 4 and 12.

To further our understanding, consider the dynamics corresponding to a more involved initial state. Till now, we have discussed the dynamics following an excitation of only a single site, the 8th site in our case. Let us assume that the initial density is defined by $\tilde{\rho}(0) = 0.5 \, |e_8\rangle\langle e_8| + 0.25 \, |e_7\rangle\langle e_7| + 0.25 \, |e_9\rangle\langle e_9|$. The system is, therefore, initially in a statistical ensemble with the 7th, 8th and 9th sites getting excited with different probabilities. The dynamics is shown in Fig. 10. The coupling between the 7th and 8th BChl units is higher than that between the 8th and 9th. This leads to a transient build-up of excitonic population in the 7th site at around 30 fs, while the population of the 9th site shows a more or less monotonic decay. Not only does the 9th BChl unit receive population from the 8th unit slowly, it also quickly leaks population into the 10th unit which is completely in the ground state because of a high elec-
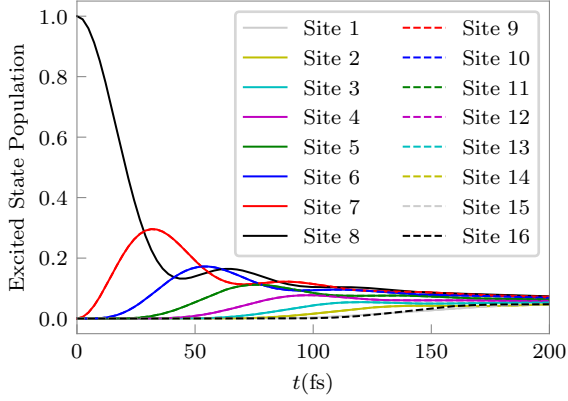
(a) BChl ring with average intermonomer electronic couplings. Excited state population of site 7 is same as that of site 9, site 6 is equal to site 10, so on.
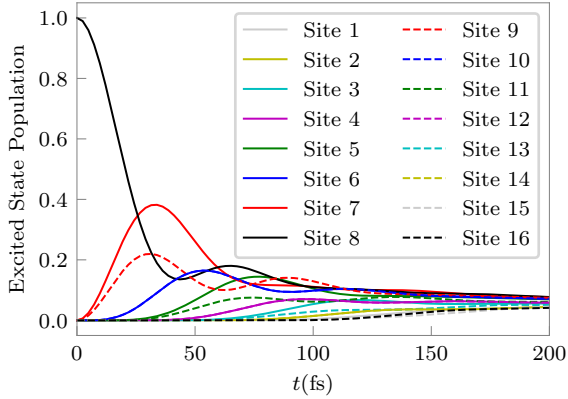
(b) Dimerized BChl ring with electronic couplings obtained using TrEsp. Data is the same as Fig. 7 but shown for a shorter time duration.

FIG. 9. Dynamics for BChl rings with identical and alternating electronic couplings.

FIG. 10. Dynamics starting from $\tilde{\rho}(0) = 0.5\,|e_8\rangle\langle e_8| + 0.25\,|e_7\rangle\langle e_7| + 0.25\,|e_9\rangle\langle e_9|$ using the TrEsp parameters.

FIG. 11. Average bond dimensions of the reduced density MPS for the B850 ring as a measure of average intersite entanglement in presence and absence of the vibrational bath.

tronic coupling.

A major consideration in multisite systems is the entanglement between the individual sites. Here, we use the average bond dimension of the reduced density MPS as a measure of the entanglement. It is intuitively quite clear that the presence of the bath should change the growth of this bond dimension and consequently the entanglement between the sites. We have shown [22] that in the case of the Ising model, the coupling to the local baths severely restricts the growth of the average bond dimension. In Fig. 11, we show the growth of the average bond dimension for the B850 system both with and without the presence of the vibrational baths. It is surprising that in this case, the average bond dimension, and consequently the intersite entanglement, of the bare B850 system does not really grow and is very small. Additionally, it is the incorporation of the vibrational bath that leads to an increase in the bond dimension. Though it must be noted that the bond dimension despite being
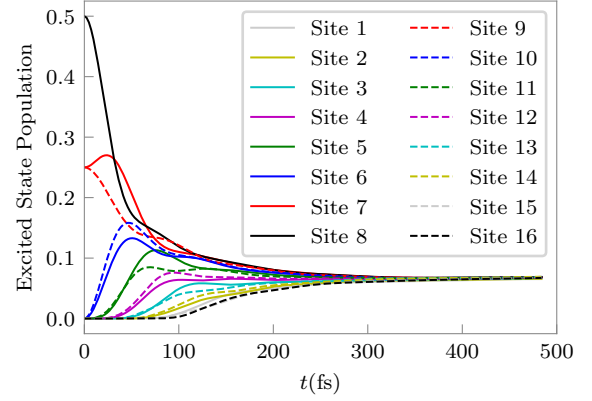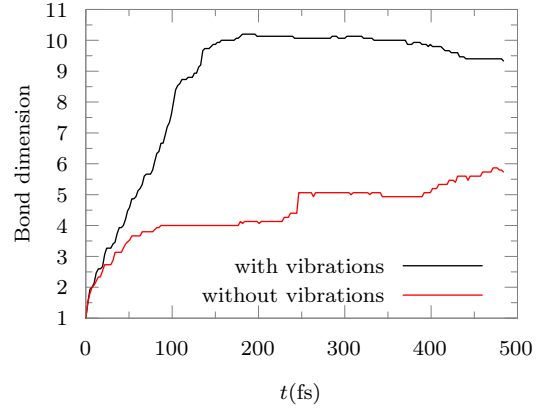
greater in presence of the bath, is still quite small. This reversal of patterns vis-à-vis the Ising model is probably unique to the Frenkel model and might be because of the block diagonal structure of the Hamiltonian. It might also arise as a consequence of the nature of the quantum transport process.

Populations do not give a full account of the dynamics as explored through experiments. We consider the absorption spectra corresponding to the two different couplings. As a zeroth order approximation, we first consider the dipole moment vectors to point in the opposite directions for neighboring monomers. The convergence parameters for these simulations are mostly the same as those used for the populations. The most notable difference being the memory span which is $L\Delta t = 33.86\,\text{fs}$ here. The correct dipole moment vectors are tangential to the B850 ring but are oriented in opposite manners [16, 52]. The mean optical excitation energy is taken to be $12\,098\,\text{cm}^{-1}$ [34]. First, we consider the spectrum corresponding to the TrEsp couplings.
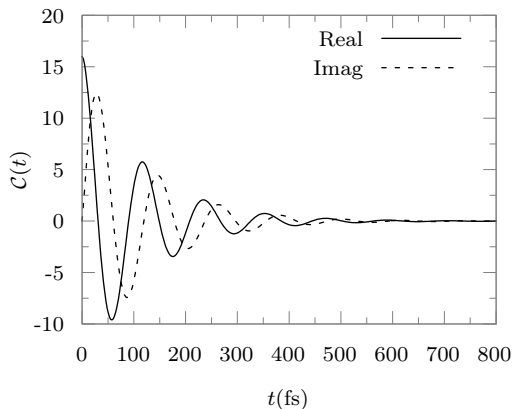
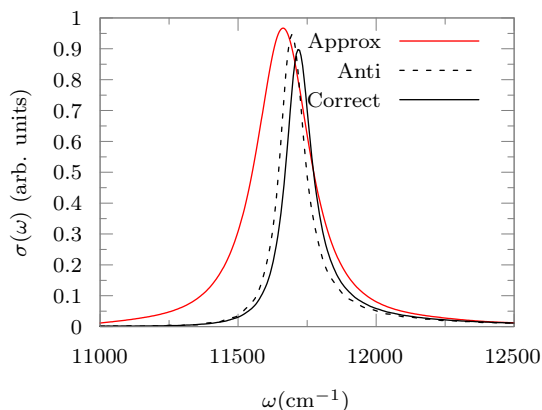FIG. 12. Correlation function after factorizing out the average excitation energy according to Eq. (28).

FIG. 13. Absorption spectrum corresponding to the TrEsp couplings and constant excitation energies. Black dashed line: antiparallel dipole moments. Black solid line: correct dipole moments. Red solid line: second-order cumulant approximation.

The dipole moment autocorrelation function without the high-frequency oscillations is demonstrated in Fig. 12. The spectra with the antiparallel dipole moments and the correct dipole moments are shown in Fig. 13. (A representative converged spectrum calculation takes roughly 2 hours on an Intel® Xeon® Gold CPU.) Along with the numerically exact MS-TNPI results, we report an approximate spectrum calculated within the second-order cumulant approximation [53].

The analysis of the absorption spectrum in terms of the Frenkel excitons is well-understood. In presence of a system with cylindrical symmetry, there are two bands of excitons as schematically demonstrated in Fig. 14 [52]. The exact energies of the excitonic eigenstates corresponding to the different system parameters is given in Appendix D. The degenerate states are labeled as $|\pm k\rangle$. The gap between the two bands is approximately $2|V_1 - V_2|$, where V_1 and V_2 are the two electronic couplings. There-
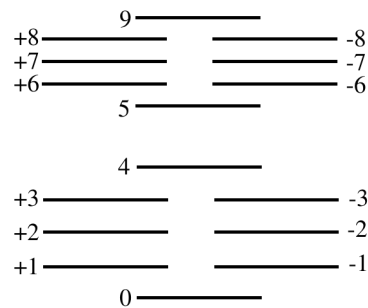

FIG. 14. Structure and spacings of the energies of the excitons for a ring with alternating couplings.

fore, if there is a constant coupling, the states $|4\rangle$ and $|5\rangle$ would be degenerate as well [16]. For the case where the dipole moments are antiparallel, the lowest energy exciton, $|0\rangle$, gets excited. However, it is well-known that the correct dipole moment actually excites into the degenerate states of $|\pm 1\rangle$ [16, 52]. Therefore, as shown in Fig. 13, we expect to see a small blue-shift of the central frequency of the peak corresponding to the correct dipole moments vis-à-vis the antiparallel ones. The excitons are coupled to each other through interactions with the site-local baths. Thus, the peak is slightly shifted and significantly broadened in the presence of the dissipative medium. The second-order cumulant approximation spectrum is quite red-shifted with respect to the correct dipole moment MS-TNPI spectrum.

Now, it is well-known that the electrostatics of the photosynthetic complex often induces a change in the excitation energies of the monomers. Typically, the excitation energy alternates with a difference of around $197 \, \mathrm{cm}^{-1}$ [16]. We have also simulated and plotted the absorption spectra corresponding to this case in Fig. 15. The incorporation of this asymmetry in the excitation energy gives rise to a smaller peak close to $12\,300 \, \mathrm{cm}^{-1}$ when using the antiparallel dipole moments. This secondary peak is caused by excitations into the highest energy exciton, $|9\rangle$, which is now permitted by the symmetry. For both the correct and antiparallel dipole moments, the main peak in the spectrum is red-shifted in comparison to the case where the monomers have the same excitation energy, due to a change in the eigenvalue spectrum. Also, it is interesting that the agreement with the approximate spectrum is much better when the varying excitation energies are incorporated.

As we had mentioned earlier, the electronic couplings obtained via TrEsp are significantly smaller than the ones derived from experiments. The same holds for the mean optical excitation energy. We calculate the absorption spectrum for the B850 ring with a mean optical excitation energy of $12\,390 \, \mathrm{cm}^{-1}$ and couplings of $315 \, \mathrm{cm}^{-1}$ and $245 \, \mathrm{cm}^{-1}$ as reported by Freiberg *et al.* [50]. The difference between the excitation energies of consecutive chlorophyll units is once again taken to be $197 \, \mathrm{cm}^{-1}$. The comparison of the spectrum corresponding to these ex-
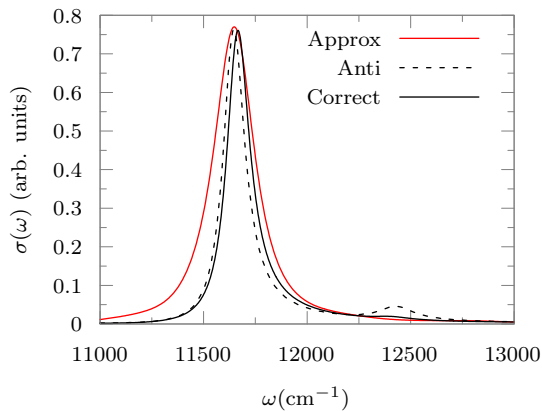
FIG. 15. Absorption spectrum corresponding to the TrEsp couplings and varying excitation energies. Black dashed line: antiparallel dipole moments. Black solid line: correct dipole moments. Red solid line: second-order cumulant approximation.

FIG. 17. Comparison of spectra at $300\,\mathrm{K}$, $150\,\mathrm{K}$ and $77\,\mathrm{K}$ for the TrEsp parameters with varying excitation energies. Effects of temperature on "solvent" spectral density has been ignored for simplicity. Solid lines: MS-TNPI spectra. Dashed lines: second-order cumulant approximation.
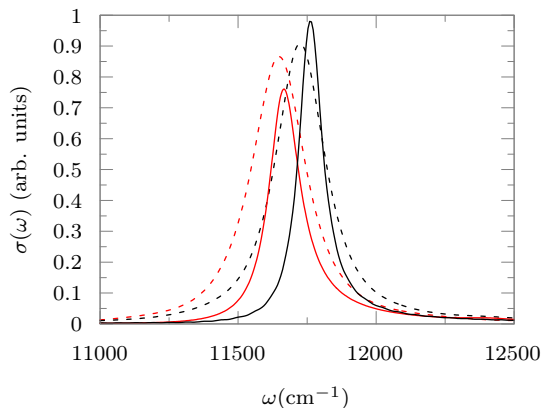

FIG. 16. Absorption spectra for TrEsp (red) and experimentally derived parameters (black) with correct dipole moments and asymmetry present. Dashed line: second-order cumulant approximation. Solid line: MS-TNPI spectra.

perimental parameters with the one corresponding to the TrEsp parameters is presented in Fig. 16. Clearly, the spectrum corresponding to the experimentally derived parameters is significantly blue-shifted with respect to the TrEsp parameters. The peak at $11\,763\,\mathrm{cm}^{-1}$ corresponds to $850.12\,\mathrm{nm}$. This is in comparison to the TrEsp parameter peak at $11\,666\,\mathrm{cm}^{-1}$ or $857.19\,\mathrm{nm}$. Because of the higher electronic couplings, the damping effect of the bath is less pronounced leading to a significantly sharper peak. It is interesting that in contrast to the MS-TNPI spectra, the peak widths of the two approximate spectra are quite similar to each other. The central frequencies of the approximate peaks have a difference of roughly $78\,\mathrm{cm}^{-1}$ between them, which is smaller than the difference between the MS-TNPI peaks. The peak of the true experimental spectrum [34] corresponding B850 region is red-shifted with respect to the TrEsp peak. This
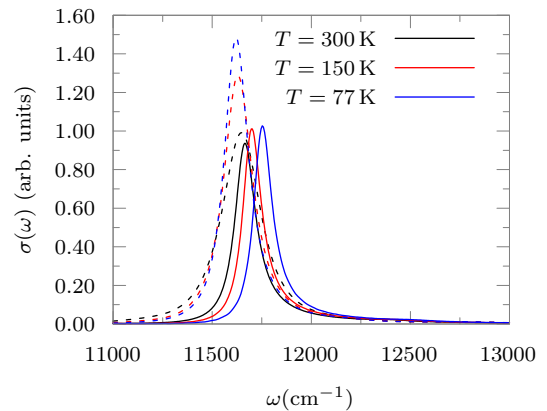
means that the agreement of the peak corresponding to the higher excitation energy and couplings with the experiment is worse than the agreement of the TrEsp peaks. Thus the effect of shielding, that leads to the smaller coupling values, are quite important.

Finally, we explore how the approximate and exact absorption spectra change with temperature. It needs to be noted that this exploration has a caveat. The spectral density coming from the protein and the rigid molecular vibrations is not necessarily independent of the temperature. The validity of the spectral density across various temperature regimes would need to be verified on a case-by-case basis. However, for simplicity, we would keep using the same spectral density across the temperatures. The spectra are calculated for the TrEsp parameters with alternating excitation energies at $300\,\mathrm{K}$, $150\,\mathrm{K}$ and $77\,\mathrm{K}$. The comparison is shown in Fig. 17. We see that as the temperature decreases, the peak of the exact spectrum gets sharper and shows a blue shift. This is consistent with observations reported by Chen *et al.* [54], though, the magnitude of the blue shift, which is dependent on the exact parameters and spectral density, is much smaller their case. The approximate spectrum peaks, on the other hand, shows a red shift while getting sharper as temperature decreases. This suggests that further investigation into various approximations for the spectra can give interesting insights into both the systems under study and the nature of the approximations.

IV. CONCLUSIONS

Understanding electronic energy transfer processes is important. However, studying the dynamics of extended systems with dissipative media is an extraordinarily challenging problem. System-solvent decomposition is a com-

monly used technique to accurately simulate open quantum systems. It handles the exponential scaling of quantum mechanics by limiting it to a small dimensional subspace. However, with such extended systems, the exponential scaling of quantum mechanics is not sufficiently curbed to allow for efficient numerical simulations. We have recently introduced MS-TNPI to address this problem using a density matrix renormalization group-like decomposition along with Feynman-Vernon influence functional. Here, we use it to study EET in a B850 ring of LH2 with vibrational spectral densities obtained using molecular dynamics. Previous numerically exact studies of the dynamics of such systems have typically been done with the Drude-Lorentz model spectral density.

In this paper, we have shown how MS-TNPI can be simply extended to account for the ring structure that is almost ubiquitous in photosynthetic complexes in purple bacteria. MS-TNPI can efficiently simulate these systems as well. While we use a "flat" 2D structure for simulating the ring system, it is conceivable that having the 2D structure turned into cylindrical form, reflecting the actual topology of the system, might bring additional computational benefits. Such ideas would be explored in the future. We have also analyzed and massaged the expressions for the absorption spectrum to make it fit for MS-TNPI. Taking advantage of the availability of the full many-body reduced density matrix for the extended system, MS-TNPI can efficiently simulate the required correlation functions and higher order response functions.

We have shown the impact of the different parameters on the direct EET dynamics in the B850 ring. The TrEsp couplings with the ZINDO/S-CIS excitation energies are generally much smaller than typical experimentally derived values. The dynamics corresponding to both cases have been simulated. The bath has similar effects on both the parameters. However, owing to the faster oscillations corresponding to the experimentally derived values, the oscillatory nature propagates even to the most distant BChl units before getting washed away. Additionally, subtle effects stemming from the unequal electronic couplings get amplified when using a more complex initial condition where multiple BChl units are statistically excited. Future work would focus on studying the impact of light on B850, taking into consideration effects stemming from the varying alignments of the site-local dipole vectors and spatial inhomogeneity of the light-BChl interaction.

Additionally, we have simulated the absorption spectrum, incorporating the full spectral density, for the ring using various approximations culminating in a simulation with the most appropriate parameters. The B850 ring is characterized by non-parallel transition dipole moments and unequal monomer excitation energies. To better understand the impact of these transition dipole moments, we started with a very simple zeroth-order approximation where the transition dipole moments are anti-parallel. We show that consistent with excitonic wave function-based analysis, if the electronic excitation energies are

identical, there is only a single peak. However, the inhomogeneities induced by the local electrostatic environment lead to a secondary peak that comes from excitation into the highest energy excitonic level. Subsequently, we analyse the effect of using the transition dipole moment with the correct form. Incorporation of the correct dipole moment operator along with the varying excitation energies still produces a spectrum that is blue-shifted with respect to experimental spectra [34]. This is probably due to inaccurate excitation energies, electronic couplings, and limitations of the model. These calculations are compared with second order cumulant approximation [53]. The approximate spectra are consistently broader than the MS-TNPI calculations, and generally slightly red-shifted. It is interesting to note that the effect of the temperature on the approximate spectra is qualitatively different from that on the exact spectra. While on decreasing the temperature, the exact spectrum shifts to higher frequencies, the approximate spectrum shifts to lower frequencies. Both the types of simulations show the sharpening of the absorption spectrum at lower temperatures. Consequences of adding static disorder to the Hamiltonian can be trivially incorporated in the MS-TNPI procedure through an external Monte Carlo averaging of separate MS-TNPI runs. A detailed exploration of such effects would be the topic of a future exploration.

MS-TNPI does not restrict the simulation to the first excitation subspace as many other methods do. These "full space" simulations, however, still remain quite simple. The singular value decompositions involved seem to be able to filter out the unnecessary information and lead to very compact representations. We simulate the dynamics corresponding to a local excitation, and show that the entanglement between the sites as calculated by the average bond dimension does not grow exponentially with time, even in the absence of the bath. This is unlike what happens in say the Ising model [22], and is probably due to the sparsity and the block-diagonal structure of the Frenkel Hamiltonian. It is also interesting that unlike the case of the Ising model where the presence of the bath controls the entanglement between different sites [22], in the case of the Frenkel-Holstein model, the presence of the bath actually serves to slightly increase the entanglement. This deserves further study.

While here we have explored the dynamics and the absorption spectra, other experimentally realizable observables can be also be simulated with similar conceptual simplicity. Further investigation of other observables, especially multi-time correlation functions and longer ranged interactions will be the focus of future work. Incorporation of long ranged interactions, through more advanced propagators (e.g., $W^{I,II}$ or TDVP based propagators), would be important in capturing dipole-dipole interactions between distant monomers in the Hamiltonian. MS-TNPI provides a flexible scheme for incorporation of increasingly complex Hamiltonians and effects of baths in a unified framework, making it a lucrative method for

studying quantum transport in extended quantum systems.

Appendix A: MS-TNPI Tensor Network

Here, we give a short outline of the exact expressions for deriving the 2D MS-TNPI tensor network [22]. The reduced density matrix of a quantum system coupled to a dissipative bath is given by the following path integral expression,

$$\tilde{\rho}(S_N^\pm, N\Delta t) = \sum_{\{S_j^\pm\}} P^{(0)}_{S_0^\pm, S_1^\pm, \ldots, S_N^\pm} \tilde{\rho}(S_0^\pm, 0) F\left[\{S_j^\pm\}\right]$$

(A1)

$$P^{(0)}_{S_0^\pm, \ldots, S_N^\pm} = K(S_N^\pm, S_{N-1}^\pm, \Delta t) \ldots K(S_1^\pm, S_0^\pm, \Delta t)$$

(A2)

where F is the Feynman-Vernon influence functional [30], $P^{(0)}$ is the bare path amplitude tensor and K is the forward-backward propagator. The system states at the nth time point are collectively denoted by $S_n^\pm$. When referring to a specific site and time point, the first index represents the spatial index and the second one the temporal index (i.e., $s_{i,n}^\pm$ corresponds to the state of the ith site at the nth time point). The forward-backward propagator is the superoperator that evolves the density matrix of the isolated system in time. It can be written as direct product of the forward, U, and backward, $U^\dagger$, system propagators,

$$K(S_n^\pm, S_{n+1}^\pm, \Delta t) = U(S_n^+, S_{n+1}^+, \Delta t)\, U^\dagger(S_n^-, S_{n+1}^-, \Delta t).$$

(A3)

There are two parts to the simulation. First, we have to need a proper representation for the forward-backward propagator. This is challenging due to the exponential growth of space requirements with the number of particles in the system. Various formalisms have been used to obtain the propagators in the compressed matrix product operator form [6, 29]. MS-TNPI can work with any of these propagators, though we have used the second-order Suzuki-Trotter split propagator.

Once the propagator has been defined, we need to include the influence functional. For that, one needs to be able to account for the non-Markovian memory induced by the bath. Usual propagations with MPO propagators simulate the Markovian dynamics in absence of solvent
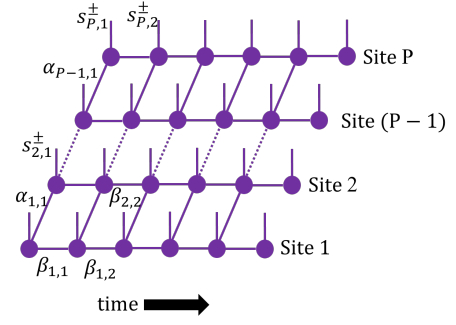

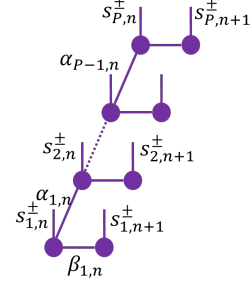FIG. 18. 2D MS-TNPI tensor network.

FIG. 19. Schematic depiction of the SVD factorization of the forward-backward propagator MPO.

modes [4, 45]. To take the memory effects into account, we need a compact tensor network representation of the bare path amplitude tensor $P^{(0)}$. This intuitively involves the construction of a grid of multiple points on the time axis. Combined with the MPO representation for the forward-backward propagator that involves a splitting along the spatial or system axis, one can visualize the formation of a 2D tensor network as shown in Fig. 18. Once this network is created, it is possible to apply the site-dependent influence functional, written as an MPO on every row of the network. In this section, we derive the formalism required for specifying and constructing the network. In Appendix B, we deal with representing the influence functional in the form of an MPO to be applied to each row.

To obtain the tensor network schematically shown in Fig. 18, we proceed by using SVD to factor the forward-backward propagator MPO as shown in Fig. 19:

$$K\left(S_n^\pm, S_{n+1}^\pm, \Delta t\right) = \sum_{\{\alpha_{(i,n)}\}} W^{s_{1,n}^\pm, s_{1,n+1}^\pm}_{\alpha_{(1,n)}} W^{s_{2,n}^\pm, s_{2,n+1}^\pm}_{\alpha_{(1,n)}, \alpha_{(2,n)}}$$
$$\cdots W^{s_{P-1,n}^\pm, s_{P-1,n+1}^\pm}_{\alpha_{(P-2,n)}, \alpha_{(P-1,n)}} W^{s_{P,n}^\pm, s_{P,n+1}^\pm}_{\alpha_{(P-1,n)}},$$

(A4)

$$W^{s_{1,n}^\pm, s_{1,n+1}^\pm}_{\alpha_{(1,n)}} = \sum_{\beta_{(1,n)}} L^{s_{1,n}^\pm}_{\alpha_{(1,n)}, \beta_{(1,n)}} R^{s_{1,n+1}^\pm}_{\beta_{(1,n)}}$$

(A5)

$$W^{s_{i,n}^\pm, s_{i,n+1}^\pm}_{\alpha_{(i-1,n)}, \alpha_{(i,n)}} = \sum_{\beta_{(i,n)}} L^{s_{i,n}^\pm}_{\alpha_{(i-1,n)}, \alpha_{(i,n)}, \beta_{(i,n)}} R^{s_{i,n+1}^\pm}_{\beta_{(i,n)}}, \; 1 < i < P$$

(A6)

$$W_{\alpha_{(P-1,n)}}^{s_{P,n}^{\pm},s_{P,n+1}^{\pm}} = \sum_{\beta_{(P,n)}} L_{\alpha_{(P-1,n)},\beta_{(P,n)}}^{s_{P,n}^{\pm}} R_{\beta_{(P,n)}}^{s_{P,n+1}^{\pm}}. \quad (A7)$$

where W are the tensors constituting the MPO representation. L and R are the factors obtained through the SVD procedure with the square root of the singular value matrix being absorbed into the factors. As per convention, the bonds along the spatial and temporal dimensions are denoted by α and β. Notice that the tensors L and R act on single system sites. By substituting the factorization for the forward-backward propagator in Eq. (A2) and regrouping terms, one can obtain the following form:

$$P_{S_0^{\pm}\cdots S_N^{\pm}}^{(0)} = \sum_{\{\beta_n\}} \mathbb{T}_{\beta_0}^{S_0^{\pm}} \cdots \mathbb{T}_{\beta_{n-1},\beta_n}^{S_n^{\pm}} \cdots \mathbb{T}_{\beta_{N-1}}^{S_N^{\pm}}. \quad (A8)$$

It is now quite simple to list the tensors constituting the MPs, $\mathbb{T}$, in Eq. (A8), in terms of L and R. In the most general case, each of these constituent tensors, represented here by M, possesses five indices: one site, $s_{i,n}^{\pm}$, and four bonds ($\alpha_{(i,n)}$, $\beta_{(i,n)}$, $\alpha_{(i-1,n)}$ and $\beta_{(i,n-1)}$), where the values of i and n correspond to the location of the tensor in the 2D grid structure. The tensors constituting the edges of the network (Fig. 18) obviously have a different topology. The tensors corresponding to the initial time point, or equivalently the first column, are given as:

$$M_{\alpha_{(1,0)},\beta_{(1,0)}}^{s_{1,0}^{\pm}} = L_{\alpha_{(1,0)},\beta_{(1,0)}}^{s_{1,0}^{\pm}} \quad (A9)$$

$$M_{\alpha_{(i,0)},\beta_{(i,0)},\alpha_{(i-1,0)}}^{s_{i,0}^{\pm}} = L_{\alpha_{(i-1,0)},\alpha_{(i,0)},\beta_{(i,0)}}^{s_{i,0}^{\pm}} \quad (A10)$$

$$M_{\alpha_{(P-1,0)},\beta_{(P,0)}}^{s_{P,0}^{\pm}} = L_{\alpha_{(P-1,0)},\beta_{(P,0)}}^{s_{P,0}^{\pm}}. \quad (A11)$$

Next, we list the expressions for the final point, last column:

$$M_{\beta_{(1,N-1)}}^{s_{1,N}^{\pm}} = R_{\beta_{(1,N-1)}}^{s_{1,N}^{\pm}} \quad (A12)$$

$$M_{\beta_{(i,N-1)}}^{s_{i,N}^{\pm}} = R_{\beta_{(i,N-1)}}^{s_{i,N}^{\pm}} \quad (A13)$$

$$M_{\beta_{(P,N-1)}}^{s_{P,N}^{\pm}} = R_{\beta_{(P,N-1)}}^{s_{P,N}^{\pm}}. \quad (A14)$$

Lastly, for an intermediate time point, n:

$$M_{\alpha_{(1,n)},\beta_{(1,n)},\beta_{(1,n-1)}}^{s_{1,n}^{\pm}} = R_{\beta_{(1,n-1)}}^{s_{1,n}^{\pm}} L_{\alpha_{(1,n)},\beta_{(1,n)}}^{s_{1,n}^{\pm}} \quad (A15)$$

$$M_{\alpha_{(i,n)},\beta_{(i,n)},\alpha_{(i-1,n)},\beta_{(i,n-1)}}^{s_{i,n}^{\pm}} = R_{\beta_{(i,n-1)}}^{s_{i,n}^{\pm}} L_{\alpha_{(i-1,n)},\alpha_{(i,n)},\beta_{(i,n)}}^{s_{i,n}^{\pm}} \quad (A16)$$

$$M_{\beta_{(P,n)},\alpha_{(P-1,n)},\beta_{(P,n-1)}}^{s_{P,n}^{\pm}} = R_{\beta_{(P,n-1)}}^{s_{P,n}^{\pm}} L_{\alpha_{(P-1,n)},\beta_{(P,n)}}^{s_{P,n}^{\pm}}. \quad (A17)$$

These expressions give a complete description of the MS-TNPI tensor network. The final step is the inclusion of the influence functional. The tensor network is ready for application of an MPO encoding the influence functional on each of the rows. The form of the influence functional MPO is given in Appendix B.

Appendix B: Influence Functional MPO

After the construction of the network, we need to be able to define the influence functional MPOs that enable the systematic incorporation of the impact of the environment on the dynamics of the system. Summarizing the results discussed in depth in Ref. [24], the full site-local influence functional, $F_i\left[\{s_{i,n}^{\pm}\}\right]$, can be factored and rewritten as a product of terms corresponding to interactions with different end-times, $F_{i,k}\left[\{s_{i,n}^{\pm}\}\right]$:

$$F_i\left[\{s_{i,n}^{\pm}\}\right] = \prod_{0 \leq k \leq N} F_{i,k}\left[\{s_{i,n}^{\pm}\}\right] \quad (B1)$$

with

$$F_{i,k}\left[\{s_{i,n}^{\pm}\}\right] = \exp\left(-\frac{1}{\hbar}\Delta s_{i,k} \sum_{0 \leq k' \leq k} (\mathrm{Re}(\eta_{kk'}^i)\Delta s_{i,k'} + 2i\,\mathrm{Im}(\eta_{kk'}^i)\bar{s}_{i,k'})\right). \quad (B2)$$

Grouping the forward-backward states of the extended system by unique values of $\Delta s_{i,k}$ allows us to represent the the influence functional associated with a particular site and end time point, $F_{i,k}\left[\{s_{i,n}^{\pm}\}\right]$, as an MPO. To see this, let us consider the case where there are b unique values of $\Delta s_{i,k}$ indexed by β. We note that for the subset of forward-backward paths where $\Delta s_{i,k} = f_i(\beta)$, we can express the influence functional, Eq. (B2), as

$$F_{i,k}(\beta) = F_{i,k}^0(\beta) \otimes F_{i,k}^1(\beta) \cdots F_{i,k}^{k-1}(\beta) \otimes F_{i,k}^k(\beta)\mathcal{P}_{f_i(\beta)}^{s_{i,k}^{\pm}}, \quad (B3)$$

where $F_{i,k}^{k'}(\beta) = e^{-\frac{1}{\hbar}f_i(\beta)\left(\mathrm{Re}(\eta_{kk'}^i)\mathbb{D}_{i,k'}+2i\,\mathrm{Im}(\eta_{kk'}^i)\mathbb{S}_{i,k'}\right)}$ is an operator that only acts on the ith site and the k'^{th} time point. In this notation $\mathcal{P}_{f_i(\beta)}^{s_{i,k}^{\pm}}$ is the projection operator on to the space where $\Delta s_{i,k} = f_i(\beta)$; additionally, $\mathbb{D}_{i,n}$ and $\mathbb{S}_{i,n}$ are diagonal matrices that represent the difference and average position of the system in the forward-backward basis, respectively. For each of the b unique value of $\Delta s_{i,k}$, the expression for the influence functional reduces to a direct product of local operators; therefore, $F_{i,k}\left[\{s_{i,n}^{\pm}\}\right]$ corresponds to a sum of direct products. Hence we can express $F_{i,k}\left[\{s_{i,n}^{\pm}\}\right]$ as a MPO, $\mathbb{F}_{i,k}$, with a bond dimension of b:

$$\mathbb{F}_{i,k} = \sum_{\{\beta_{(i,n)}\}} W_{\beta_{(i,0)}}^{s_{i,0}^{\pm},s_{i,0}'^{\pm}}(\eta_{k0}^i) \cdots W_{\beta_{(i,k'-1)},\beta_{(i,k')}}^{s_{i,k'}^{\pm},s_{i,k'}'^{\pm}}(\eta_{kk'}^i)$$
$$\times W_{\beta_{(i,k')},\beta_{(i,k'+1)}}^{s_{i,k'+1}^{\pm},s_{i,k'+1}'^{\pm}}(\eta_{k(k'+1)}^i) \cdots W_{\beta_{(i,k-1)}}^{s_{i,k}^{\pm},s_{i,k}'^{\pm}}(\eta_{kk}^i) \quad (B4)$$

Here, W are the various tensors constituting our influence functional MPO, and are defined as:

$$W^{s_{i,0}^\pm, s_{i,0}^{\prime\pm}}_{\beta_{(i,0)}}(\eta^i_{k0}) = \delta_{s_{i,0}^\pm, s_{i,0}^{\prime\pm}} \exp\left(-\tfrac{1}{\hbar} f_i(\beta_{(i,0)})(\mathrm{Re}(\eta^i_{k0})\Delta s_{i,0} + 2i\,\mathrm{Im}(\eta^i_{k0})\bar{s}_{i,0})\right) \tag{B5}$$

$$W^{s_{i,k'}^\pm, s_{i,k'}^{\prime\pm}}_{\beta_{(i,k'-1)}, \beta_{(i,k')}}(\eta^i_{kk'}) = \delta_{s_{i,k'}^\pm, s_{i,k'}^{\prime\pm}} \delta_{\beta_{(i,k'-1)}, \beta_{(i,k')}} \exp\left(-\tfrac{1}{\hbar} f_i(\beta_{(i,k'-1)})(\mathrm{Re}(\eta^i_{kk'})\Delta s_{i,k'} + 2i\,\mathrm{Im}(\eta^i_{kk'})\bar{s}_{i,k'})\right) \tag{B6}$$

$$W^{s_{i,k}^\pm, s_{i,k}^{\prime\pm}}_{\beta_{(i,k-1)}}(\eta^i_{kk}) = \delta_{s_{i,k}^\pm, s_{i,k}^{\prime\pm}} \mathcal{P}^{s_{i,k}^\pm}_{f_i(\beta_{(i,k-1)})} \exp\left(-\tfrac{1}{\hbar}\Delta s_{i,k}(\mathrm{Re}(\eta^i_{kk})\Delta s_{i,k} + 2i\,\mathrm{Im}(\eta^i_{kk})\bar{s}_{i,k})\right) \tag{B7}$$

It's worth noting that the primed forward-backward indices that appear in Eqs. (B4)–(B7) are necessary for bookkeeping purposes only. Computationally, for any particular time-step, we only apply the $\mathbb{F}_{i,n}$ operators corresponding to the final time point. This procedure leads to a sequential or iterative build-up of the full influence functional including the effects arising from all the intermediate points.

Appendix C: Total Dipole Moment MPO

In the paper, we have outlined a general idea about how to calculate the MPO representation for the total dipole operator as a sum of individual MPOs. However, it is possible to represent it as an MPO in an exact manner without resorting to MPO summations. In this appendix, we outline the basic formulae involved in deriving a low bond-dimensioned MPO representation for the operator.

Consider the initial "state" involved in the absorption spectrum:

$$C(t) = \mathrm{Tr}(\hat{\mu}(t)\hat{\mu}(0)\rho(0)). \tag{C1}$$

The $\hat{\mu}$ operator acts on the forward space or on the ket side. We can formulate an MPO which is a delta function on the bra side and the total dipole operator on the ket side. This MPO is denoted by $\bar{\bar{\mu}}^+$. The superscript "+" denotes that the total dipole acts on the forward space.

$$\bar{\bar{\mu}}^+ = \sum_{\{\alpha_i\}} W^{s_1^\pm, s_1^{\prime\pm}}_{\alpha_1} W^{s_2^\pm, s_2^{\prime\pm}}_{\alpha_1, \alpha_2} \cdots W^{s_{P-1}^\pm, s_{P-1}^{\prime\pm}}_{\alpha_{P-2}, \alpha_{P-1}} W^{s_P^\pm, s_P^{\prime\pm}}_{\alpha_{P-1}} \tag{C2}$$

where W are the constituent tensors of the MPO. The site indices are $s_i^\pm$ and $s_i^{\pm'}$. The intuition is that $s_i^\pm$ are the "input" indices and $s_i^{\prime\pm}$ are the output indices. The primes have no other semantic meaning. The bond index connecting the ith and $(i+1)^{\text{th}}$ are denoted by α_i.

Below we list the explicit formulae for the W tensors.

$$W^{s_1^\pm, s_1^{\prime\pm}}_{\alpha_1} = \begin{cases} \left\langle s_1^{\prime+} \middle| \hat{\mu}_1 \middle| s_1^+ \right\rangle \delta_{s_1^-, s_1^{\prime-}}, & \alpha_1 = 0 \\ \delta_{s_1^\pm, s_1^{\prime\pm}}, & \alpha_1 = 1 \end{cases} \tag{C3}$$

$$W^{s_i^\pm, s_i^{\prime\pm}}_{\alpha_{i-1}, \alpha_i} = \begin{cases} \delta_{s_i^\pm, s_i^{\prime\pm}}, & \alpha_{i-1} = \alpha_i \\ \left\langle s_i^{\prime+} \middle| \hat{\mu}_i \middle| s_i^+ \right\rangle \delta_{s_i^-, s_i^{\prime-}}, & \alpha_{i-1} = 1 \text{ and } \alpha_i = 0 \\ 0, & \text{otherwise} \end{cases} \tag{C4}$$

$$W^{s_P^\pm, s_P^{\prime\pm}}_{\alpha_{P-1}} = \begin{cases} \delta_{s_P^\pm, s_P^{\prime\pm}}, & \alpha_{P-1} = 1 \\ \left\langle s_P^{\prime+} \middle| \hat{\mu}_P \middle| s_P^+ \right\rangle \delta_{s_P^-, s_P^{\prime-}}, & \alpha_{P-1} = 0 \end{cases} \tag{C5}$$

Note that since the bond indices only take two values (0 or 1), the bond dimension of this analytical dipole moment MPO is exactly 2.

Appendix D: Excitonic Eigenstates

In the main text, we discussed three different system parameter sets in the context of the absorption spectrum. We dealt with the TrEsp parameters, with and without the $197\,\mathrm{cm}^{-1}$ variation in the excitation energies of neighboring BChl units, and the experimentally derived parameters with the variation. Here we list the energies of the excitonic eigenstates for all three parameters. These eigen-energies do not account for the solvent interaction at all.

State	TrEsp	TrEsp	Experimental
No.	w/o Variation	w/ Variation	w/ Variation
0	11679.5	11664.4	11715.4
±1	11703.1	11686.8	11756.6
±2	11770.0	11749.1	11872.9
±3	11868.9	11834.5	12039.4
4	11959.5	11888.6	12163.1
5	12025.5	12096.4	12404.8
±6	12116.1	12150.6	12528.5
±7	12215.1	12235.9	12695.0
±8	12282.0	12298.3	12811.3
9	12305.5	12320.7	12852.6

TABLE I. Energies for the excitonic eigenstates in absence of coupling to the thermal environment.

[1] A. Ishizaki and G. R. Fleming, On the adequacy of the Redfield equation and related approaches to the study of quantum dynamics in electronic energy transfer, J.

Chem. Phys. **130**, 234110 (2009).

[2] V. Novoderezhkin and A. Razjivin, The theory of forster-type migration between clusters of strongly interacting molecules: application to light-harvesting complexes of purple bacteria, Chemical Physics **211**, 203 (1996).

[3] S. R. White, Density matrix formulation for quantum renormalization groups, Phys. Rev. Lett. **69**, 2863 (1992).

[4] S. R. White and A. E. Feiguin, Real-Time Evolution Using the Density Matrix Renormalization Group, Phys. Rev. Lett. **93**, 10.1103/physrevlett.93.076401 (2004).

[5] U. Schollwöck, The density-matrix renormalization group, Rev. Mod. Phys. **77**, 259 (2005).

[6] U. Schollwöck, The density-matrix renormalization group in the age of matrix product states, Ann. Phys. (N. Y.) **326**, 96 (2011).

[7] T. Jiang, W. Li, J. Ren, and Z. Shuai, Finite Temperature Dynamical Density Matrix Renormalization Group for Spectroscopy in Frequency Domain, J. Phys. Chem. Lett. **11**, 3761 (2020).

[8] M. Beck, The multiconfiguration time-dependent Hartree (MCTDH) method: A highly efficient algorithm for propagating wavepackets, Physics Reports **324**, 1 (2000).

[9] H. Wang and M. Thoss, Multilayer formulation of the multiconfiguration time-dependent Hartree theory, J. Chem. Phys. **119**, 1289 (2003).

[10] J. Ren, Z. Shuai, and G. Kin-Lic Chan, Time-Dependent Density Matrix Renormalization Group Algorithms for Nearly Exact Absorption and Fluorescence Spectra of Molecular Aggregates at Both Zero and Finite Temperature, J. Chem. Theory Comput. **14**, 5027 (2018).

[11] Y. Tanimura, Numerically "exact" approach to open quantum dynamics: The hierarchical equations of motion (HEOM), J. Chem. Phys. **153**, 020901 (2020).

[12] Y. Tanimura and R. Kubo, Time Evolution of a Quantum System in Contact with a Nearly Gaussian-Markoffian Noise Bath, J. Phys. Soc. Jpn. **58**, 101 (1989).

[13] Y. Yan, M. Xu, T. Li, and Q. Shi, Efficient propagation of the hierarchical equations of motion using the Tucker and hierarchical Tucker tensors, J. Chem. Phys. **154**, 194104 (2021).

[14] N. Makri and D. E. Makarov, Tensor propagator for iterative quantum time evolution of reduced density matrices. I. Theory, J. Chem. Phys. **102**, 4600 (1995).

[15] N. Makri and D. E. Makarov, Tensor propagator for iterative quantum time evolution of reduced density matrices. II. Numerical methodology, J. Chem. Phys. **102**, 4611 (1995).

[16] J. Strümpfer and K. Schulten, Light harvesting complex II B850 excitation dynamics, J. Chem. Phys. **131**, 225101 (2009).

[17] J. Strümpfer and K. Schulten, The effect of correlated bath fluctuations on exciton transfer, J. Chem. Phys. **134**, 095102 (2011).

[18] J. Strümpfer and K. Schulten, Excited state dynamics in photosynthetic reaction center and light harvesting complex 1, J. Chem. Phys. **137**, 065101 (2012).

[19] N. Makri, Modular path integral methodology for real-time quantum dynamics, J. Chem. Phys. **149**, 214108 (2018).

[20] S. Kundu and N. Makri, Real-Time Path Integral Simulation of Exciton-Vibration Dynamics in Light-Harvesting Bacteriochlorophyll Aggregates, J. Phys. Chem. Lett. **11**, 8783 (2020).

[21] S. Kundu and N. Makri, Origin of vibrational features in the excitation energy transfer dynamics of perylene bisimide J-aggregates, J. Chem. Phys. **154**, 114301 (2021).

[22] A. Bose and P. L. Walters, A multisite decomposition of the tensor network path integrals, J. Chem. Phys. **156**, 24101 (2022).

[23] M. K. Lee, P. Huo, and D. F. Coker, Semiclassical Path Integral Dynamics: Photosynthetic Energy Transfer with Realistic Environment Interactions, Annu. Rev. Phys. Chem. **67**, 639 (2016).

[24] A. Bose and P. L. Walters, A tensor network representation of path integrals: Implementation and analysis, arXiv pre-print server (2021).

[25] A. Bose, Pairwise connected tensor network representation of path integrals, Phys. Rev. B **105**, 024309 (2022).

[26] A. Strathearn, P. Kirton, D. Kilda, J. Keeling, and B. W. Lovett, Efficient non-Markovian quantum dynamics using time-evolving matrix product operators, Nat. Commun **9**, 10.1038/s41467-018-05617-3 (2018).

[27] M. R. Jørgensen and F. A. Pollock, Exploiting the Causal Tensor Network Structure of Quantum Processes to Efficiently Simulate Non-Markovian Path Integrals, Phys. Rev. Lett. **123**, 10.1103/physrevlett.123.240602 (2019).

[28] U. Schollwöck, The density-matrix renormalization group: A short introduction, Philos. Trans. A Math. Phys. Eng. Sci. **369**, 2643 (2011).

[29] S. Paeckel, T. Köhler, A. Swoboda, S. R. Manmana, U. Schollwöck, and C. Hubig, Time-evolution methods for matrix-product states, Ann. Phys. (N. Y.) **411**, 167998 (2019).

[30] R. P. Feynman and F. L. Vernon, The theory of a general quantum system interacting with a linear dissipative system, Ann. Phys. (N. Y.) **24**, 118 (1963).

[31] A. Ishizaki and G. R. Fleming, Theoretical examination of quantum coherence in a photosynthetic system at physiological temperature, Proc. Natl. Acad. Sci. **106**, 17255 (2009).

[32] M. Rätsep and A. Freiberg, Electron–phonon and vibronic couplings in the FMO bacteriochlorophyll a antenna complex studied by difference fluorescence line narrowing, J. Lumin. **127**, 251 (2007).

[33] A. Bose and N. Makri, All-Mode Quantum–Classical Path Integral Simulation of Bacteriochlorophyll Dimer Exciton-Vibration Dynamics, J. Phys. Chem. B **124**, 5028 (2020).

[34] C. Olbrich and U. Kleinekathöfer, Time-Dependent Atomistic View on the Electronic Relaxation in Light-Harvesting System II, J. Phys. Chem. B **114**, 12427 (2010).

[35] C. Olbrich, J. Strümpfer, K. Schulten, and U. Kleinekathöfer, Theory and Simulation of the Environmental Effects on FMO Electronic Transitions, J. Phys. Chem. Lett. **2**, 1771 (2011).

[36] S. Maity, B. M. Bold, J. D. Prajapati, M. Sokolov, T. Kubař, M. Elstner, and U. Kleinekathöfer, DFTB/MM Molecular Dynamics Simulations of the FMO Light-Harvesting Complex, J. Phys. Chem. Lett. **11**, 8660 (2020).

[37] A. O. Caldeira and A. J. Leggett, Path integral approach to quantum Brownian motion, Physica A: Statistical Mechanics and its Applications **121**, 587 (1983).

[38] N. Makri, The Linear Response Approximation and Its Lowest Order Corrections: An Influence Functional Ap-

proach, J. Phys. Chem. B **103**, 2823 (1999).

[39] H. Kim and P. J. Rossky, Evaluation of Quantum Correlation Functions from Classical Data, J. Phys. Chem. B **106**, 8240 (2002).

[40] H. Kim and P. J. Rossky, Evaluation of quantum correlation functions from classical data: Anharmonic models, The Journal of Chemical Physics **125**, 074107 (2006), https://doi.org/10.1063/1.2274412.

[41] S. Valleau, A. Eisfeld, and A. Aspuru-Guzik, On the alternatives for bath correlators and spectral densities from mixed quantum-classical simulations, J. Chem. Phys. **137**, 224103 (2012).

[42] M. K. Lee and D. F. Coker, Modeling Electronic-Nuclear Interactions for Excitation Energy Transfer Processes in Light-Harvesting Complexes, J. Phys. Chem. Lett. **7**, 3171 (2016).

[43] A. J. Daley, C. Kollath, U. Schollwöck, and G. Vidal, Time-dependent density-matrix renormalization-group using adaptive effective Hilbert spaces, J. Stat. Mech. Theory Exp. **2004**, P04005 (2004).

[44] J. Haegeman, J. I. Cirac, T. J. Osborne, I. Pižorn, H. Verschelde, and F. Verstraete, Time-Dependent Variational Principle for Quantum Lattices, Phys. Rev. Lett. **107**, 070601 (2011).

[45] M. Yang and S. R. White, Time-dependent variational principle with ancillary Krylov subspace, Phys. Rev. B **102**, 094315 (2020).

[46] M. P. Zaletel, R. S. K. Mong, C. Karrasch, J. E. Moore, and F. Pollmann, Time-evolving a matrix product state with long-ranged interactions, Phys. Rev. B **91**, 165112 (2015).

[47] G. Vidal, Efficient Simulation of One-Dimensional Quantum Many-Body Systems, Phys. Rev. Lett. **93**, 040502 (2004).

[48] T. Renger, Theory of excitation energy transfer: from structure to function, Photosynth. Res. **102**, 471 (2009).

[49] M. E. Madjet, A. Abdurahman, and T. Renger, Intermolecular Coulomb Couplings from Ab Initio Electrostatic Potentials: Application to Optical Transitions of Strongly Coupled Pigments in Photosynthetic Antennae and Reaction Centers, J. Phys. Chem. B **110**, 17268 (2006).

[50] A. Freiberg, M. Rätsep, K. Timpmann, and G. Trinkunas, Excitonic polarons in quasi-one-dimensional lh1 and lh2 bacteriochlorophyll a antenna aggregates from photosynthetic bacteria: A wavelength-dependent selective spectroscopy study, Chemical Physics **357**, 102 (2009), excited State Dynamics in Light Harvesting Materials.

[51] S. Tretiak, C. Middleton, V. Chernyak, and S. Mukamel, Bacteriochlorophyll and Carotenoid Excitonic Couplings in the LH2 System of Purple Bacteria, J. Phys. Chem. B **104**, 9540 (2000).

[52] X. Hu, T. Ritz, A. Damjanović, and K. Schulten, Pigment Organization and Transfer of Electronic Excitation in the Photosynthetic Unit of Purple Bacteria, J. Phys. Chem. B **101**, 3854 (1997).

[53] A. Damjanovići, I. Kosztin, U. Kleinekathöfer, and K. Schulten, Excitons in a photosynthetic light-harvesting system: A combined molecular dynamics, quantum chemistry, and polaron model study, Phys. Rev. E **65**, 31919 (2002).

[54] L. Chen, R. Zheng, Q. Shi, and Y. Yan, Optical line shapes of molecular aggregates: Hierarchical equations of motion method, J. Chem. Phys. **131**, 94502 (2009).